fluids

MDPI

Article

Effects of Nozzle Geometry on Fine Bubble Generation and Surface Cleaning Performance

Xin Jiang [1,*], Ryota Matoyama [1], Yumiko Otobe [1], Masaki Shimazu [1] and Satoru Ogahara [2,3]

[1] National Institute of Technology, Kitakyushu College, Fukuoka 802-0985, Japan; ad2417ru@apps.kct.ac.jp (R.M.); otobe@apps.kct.ac.jp (Y.O.); shimazu@kct.ac.jp (M.S.)
[2] Hoyo Seisakusho Co., Ltd., 1-44 Torigoe-cho, Kanda-machi, Fukuoka 800-0304, Japan; s.ogahara.dt@adm.fukuoka-u.ac.jp
[3] Faculty of Engineering, Fukuoka University, 8-19-1 Nanakuma, Jonan-ku, Fukuoka 814-0180, Japan
* Correspondence: jiangxin@kct.ac.jp; Tel.: +81-093-964-7298

Abstract

Fine bubbles have attracted attention in recent years due to their promising characteristics and extensive applications. One type of fine bubble generator, the Venturi tube, utilizes a sudden change in pressure inside the tube and is widely used due to its simple structure, high generation efficiency, and low power consumption. The volume of bubbles generated (generation yield) and their average diameter are key parameters in evaluating the performance of a Venturi tube generator, which depends on both the flow conditions and the geometric configuration of the generator. In this study, an oral irrigator incorporating fine bubble technology was developed, with a Venturi tube embedded in the irrigator for fine bubble generation. We designed Venturi tubes with various geometric configurations under different flow conditions to enhance fine bubble generation performance and cleaning efficiency through both experiments and numerical simulations. The results indicate that the generation performance and cleaning performance of fine bubbles are strongly influenced by the geometric parameters of the Venturi tube. Among the tested configurations, the Venturi tube with a divergent angle of 5° and a divergent length of 30 mm demonstrated the best performance.

Keywords: Venturi tube; fine bubble; flow state; geometrical combination; numerical simulation

Check for updates

Academic Editors: Manolis Gavaises, Van-Tu Nguyen and Hemant J. Sagar

Received: 28 January 2026
Revised: 18 February 2026
Accepted: 24 February 2026
Published: 27 February 2026

Copyright: © 2026 by the authors. Licensee MDPI, Basel, Switzerland. This article is an open access article distributed under the terms and conditions of the Creative Commons Attribution (CC BY) license.

1. Introduction

Fine bubbles—commonly defined as gas bubbles with diameters below 100 μm—exhibit a high specific interfacial area and distinct physicochemical effects that have strong cleaning, sterilizing, and physiologically active effects and are applied in various industrial fields [1]. Among various generation methods, Venturi tube bubble generators are particularly attractive because they combine a simple structure with low energy consumption while producing fine bubbles through rapid pressure reduction at the throat, followed by pressure recovery in the divergent section. The sudden pressure drop promotes air entrainment, and the subsequent shear, turbulence, and gas–liquid interfacial instabilities drive bubble breakup and the formation of smaller bubbles in two-phase flow [2,3]. As shown in Figure 1, a Venturi tube is composed of three parts: the convergent, throat, and divergent parts.

The geometry of a Venturi tube is a primary determinant of bubble formation characteristics. Prior studies have shown that geometric parameters—such as the throat diameter,

the divergent angle, and the length of the divergent section—influence local turbulence intensity and the spatial distribution of breakup/coalescence events, thereby controlling both the volume and the size distribution of generated bubbles [4–6]. Many studies [7–10] have proved that the performance of the generator is highly dependent on the geometric parameters, especially the divergent angle α and the throat ratio. The throat ratio is defined as the ratio of the throat diameter d to the outlet (or downstream) diameter D, i.e.,

$$\text{throat ratio} = \frac{d}{D} \tag{1}$$

While some works report modest sensitivity to diffuser geometry for specific operating ranges, others demonstrate sizeable reductions in mean bubble size as the divergent angle or liquid Reynolds number increases, underscoring that scale, operating regime, and air–water loading critically mediate geometric effects [10,11]. Nevertheless, most investigations to date have focused on relatively large-scale configurations, and systematic evidence for miniature Venturi tubes intended for compact devices remains limited.

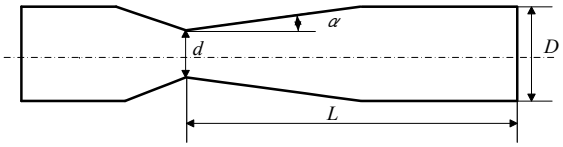

Figure 1. Geometric parameters of the Venturi tube. This figure illustrates the main geometric dimensions of the Venturi tube, including the inlet diameter, throat diameter, outlet diameter, diverging angles, and the lengths of the divergent section. These parameters influence local turbulence intensity and the spatial distribution of breakup/coalescence events, thereby controlling both the volume and the size distribution of generated bubbles.

Fine-bubble-assisted oral cleaning devices, such as oral irrigators, demand compact generators that can produce high concentrations of small bubbles under strict constraints on nozzle diameter and overall length. Clinical literature shows mixed but relevant evidence regarding oral irrigators' cleansing efficacy relative to flossing—often depending on anatomical accessibility and user compliance—highlighting the need to better link bubble attributes to cleaning outcomes [12,13]. Despite rising interest, the influence of miniature Venturi geometry on fine bubble generation for oral irrigators has not been sufficiently clarified. In particular, quantitative relationships between bubble attributes (e.g., size and concentration) and cleaning performance remain under-established due to limited coupled experimental–numerical datasets [12,13].

Therefore, the objective of this study is to elucidate how the geometric parameters of miniature Venturi tubes affect fine bubble generation and surface cleaning performance under the dimensional constraints of an oral irrigator. We designed Venturi tubes with different geometrical combinations to improve the performance of fine bubble generation, including bubble size and volume. To be embedded in the oral irrigator, the nozzle diameter should be within 20 mm, and the total length should be 50 mm or less. In order to find the effect of the geometric parameters on the fine bubble generation performance, we designed Venturi tubes with different parameter combinations. We fix the throat diameter to 1 mm and change the divergent angles from 1.2° to 12.5°, and the throat downstream length is changed L from 10 mm to 40 mm, and the diameter of the outlet D and the throat ratio are changed correspondingly. The geometric parameters tested in this work are shown in Table 1.

The Venturi tube nozzles were produced using a Form 3B 3D printer with transparent resin, and experiments were conducted to visualize the generated fine bubbles and evaluate their cleaning performance. The produced nozzles for the experiment are shown in Figure 2.

The experimental program quantifies visible and invisible bubbles through image-based bubble area ratios, minimum visible diameters, and NanoSight-based [14] nanobubble concentrations, following nanoparticle tracking analysis (NTA) protocols, and evaluates cleaning performance via removal efficiency tests [15,16]. In parallel, we performed three-dimensional, two-phase flow simulations using a volume-of-fluid framework coupled with a population balance model (PBM) employing a widely used breakup kernel (Luo model) to analyze the internal flow state, breakup dynamics, and turbulence distribution [17–21]. By correlating experimental observations with numerical predictions, this study identifies geometry combinations that enhance generation efficiency and cleaning performance, providing actionable guidance for designing fine-bubble-based oral cleaning devices.

Table 1. Geometric parameters of the Venturi tube tested in this work.

No.	Divergent Angle α°	Throat Diameter d mm	Outlet Diameter D mm	Throat Downstream Length L mm
1	1.2	1	2.7	40
2	2.5	1	2.7	20
3	2.5	1	4.5	40
4	5	1	2.7	10
5	5	1	4.5	20
6	5	1	6.2	30
7	5	1	8	40
8	7.5	1	3.6	10
9	7.5	1	6.3	20
10	7.5	1	8.9	30
11	7.5	1	11.5	40
12	10	1	4.5	10
13	10	1	8.0	20
14	10	1	11.6	30
15	12.5	1	5.4	10
16	12.5	1	9.9	20



Figure 2. High-resolution photographs of the 3D-printed Venturi tube nozzles used in the experiments. All nozzles were fabricated using a Form 3B 3D printer with transparent resin. The images have been enlarged and enhanced to clearly show the geometry of each nozzle, including the convergent, throat, and divergent sections.

2. Experimental and Simulation Conditions

2.1. Experimental Conditions

The schematic diagram of the experimental apparatus is shown in Figure 3, and a picture of the experiment site is shown in Figure 4. The working fluid used in the experiments is tap water. The nozzle is installed in a water reservoir, and water is supplied by a variable water flow pump to generate bubbles. A flow meter is attached to the pipe connecting the pump and the inlet of the nozzle to measure the supply flow of tap water into the nozzle, and the inlet flow rate Q_w is regulated from 1 L/min to 3 L/min. Bubbles are generated from each nozzle, and the flow states in the nozzle are photographed with a high-speed camera, k8-USB (Kato Koken Co., Ltd., Kanagawa, Japan). A part of the reservoir full of generated fine bubbles is photographed, and the picture is implemented with binarization processing. A sample of the pictures before and after binarization processing is shown in Figure 5a,b. After binarization processing, the black background is considered as water, and the white parts are bubbles. The area ratios of the bubbles in the tank are calculated by dividing the area of the white part by the black part to analyze the production volume of the bubbles. Then, the states of the water reservoir full of fine bubbles are photographed by a microscope L-KIT652 (HOZAN Co., Ltd., Osaka, Japan), and the particle size of the generated fine bubbles is measured from the pictures taken by the microscope. The experimental nozzles were fabricated by SLA 3D printing (Form 3B, transparent resin) (Formlabs, Somerville, MA, USA). By contrast, mass-manufactured nozzles typically exhibit lower Ra and tighter dimensional tolerances. Surface roughness can modify boundary-layer development and local wall shear, potentially altering air entrainment and breakup/coalescence rates.

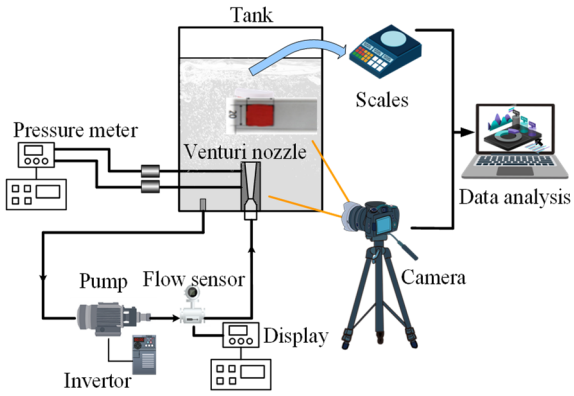

Figure 3. Schematic diagram of the experimental apparatus.

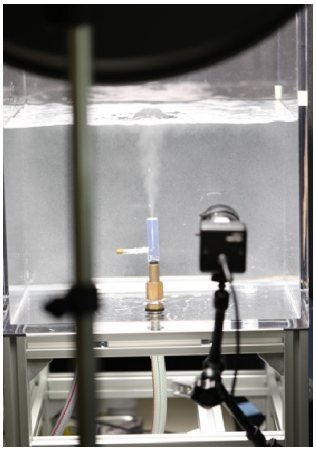

Figure 4. Picture of the experiment site.

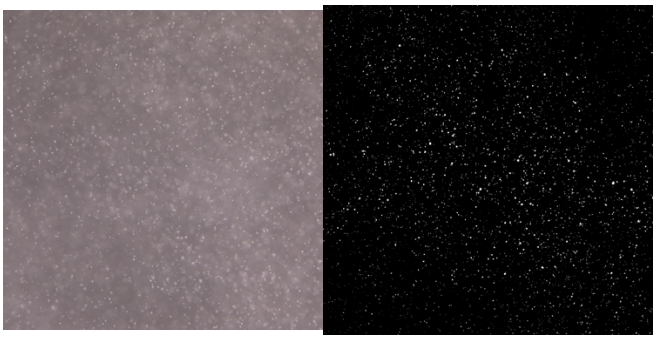

(**a**) (**b**)

Figure 5. Example images of the reservoir filled with fine bubbles and the corresponding binarization process. (**a**) Original grayscale image acquired under fixed illumination and exposure; (**b**) binarized image used for area-based quantification, where white pixels indicate bubbles and black pixels indicate water.

To analyze the particle distributions of the invisible bubbles, a nanoparticle analysis system, Nanosight, is used, which can measure the particles ranging from 10 to 1000 nm. The particle size, distribution, and concentration of the generated nanobubbles were measured and analyzed.

To evaluate the cleaning performance of fine bubbles, preparations with poster color are placed into the reservoir filled with fine bubbles. The weight of the preparations before and after cleaning is measured using a high-precision scale, and the removal rate of the poster color is calculated, which serves as the index to evaluate the cleaning capacity. The removal rates of water without fine bubbles and water with fine bubbles, as well as those of different nozzles, are compared.

2.2. Simulation Conditions

In the numerical simulation, blocking meshes were created in ICEM CFD, and 3D CFD simulations were performed with the ANSYS Fluent R1 Volume of Fluid (VOF) Compressible Two-Phase Flow-Population Balance Module to analyze internal flow conditions and evaluate generation performance. The SST k-ω turbulence model was implemented for the calculations. In the Population Balance Module, we utilize the Luo model for a balance equation to describe the changes in the particle population, in addition to momentum, mass, and energy balances, and the aggregation and breakage producing the dispersion evolutionary processes [9] are considered in the model. The numerical simulations were conducted using the incompressible two-phase Navier–Stokes equations with the VOF method to track the gas–liquid interface. The governing equations consist of the continuity equation and the momentum equation:

$$\nabla \cdot u = 0 \tag{2}$$

$$\rho\left(\frac{\partial u}{\partial t} + u \cdot \nabla u\right) = -\nabla p + \nabla \cdot (\mu \nabla u) + \rho g \tag{3}$$

where ρ and μ represent the mixture density and viscosity computed based on the gas–liquid volume fraction.

Water was treated as an incompressible fluid with constant density and viscosity. The density and dynamic viscosity were set to 998 kg/m^3 and 1.0×10^{-3} Pa·s, respectively. Air density and viscosity were set to 1.2 kg/m^3 and 1.8×10^{-5} Pa·s. The simulations were performed with ANSYS Fluent using the pressure-based solver. The VOF method with geometric reconstruction was used for interface capturing. The SST k-ω model was employed for turbulence modeling. Second-order upwind schemes were applied to momentum and

turbulent quantities, and the PISO algorithm was used for pressure–velocity coupling. The convergence criteria were set to 10^{-5} for all residuals. The boundary conditions for the simulation are shown in Table 2. These conditions correspond exactly to the flow rates and pressure conditions used in the experiment. Our CFD model assumed hydraulically smooth walls; therefore, roughness-induced pressure losses and turbulence augmentation are not captured and may explain part of the discrepancy between simulations and experiments. We include this as a limitation and a direction for future work, where rough-wall modeling and/or wall functions could be introduced.

Table 2. Boundary conditions for the numerical simulation.

Model	Two-Phase Flow-Population Balance
Calculation function	SST-k-ω
Particle diameters	0.001 mm, 0.003 mm, 0.006 mm, 0.016 mm, 0.04 mm, 0.102 mm, 0.256 mm, 0.645 mm, 1.626 mm, 4.096 mm
Breakup model	Luo model
State of wall	No slip
Air inlet	p = 101.325 kPa, velocity inlet (1.0 m/s, void fraction = 0.2)
Water inlet	p = 210 kPa, velocity inlet (2.1 m/s)
Outlet	pressure outlet (101.325 kPa)

3. Experimental Results and Analysis

We conducted several experiments on the Venturi tube nozzles with different geometric parameters. First, to analyze the relationship between the parameters and the bubble volume, we placed different nozzles in the tank, and the area ratios of the bubbles were calculated. Then, the particle properties of nanobubbles were tested and analyzed. Finally, the cleaning performance of fine bubbles was evaluated through a cleaning experiment. For several figures, replicate measurements could not be recovered at the time of revision due to data management issues. To avoid reporting misleading statistics, these results are presented as single-point estimates without error bars. Where applicable for image-based metrics, we additionally report a threshold-sensitivity analysis that reflects methodological uncertainty rather than experimental variability.

3.1. Experiments of Visible Bubble Measurement

To quantify the visible bubble volume, the captured tank images were binarized, with white pixels representing bubbles and black pixels representing water. The bubble area ratio is defined as the ratio of the projected bubble area to the projected water area. Although this is a two-dimensional projection, all images were recorded at a fixed measurement time (t = 60 s), which was verified in preliminary tests to avoid time-dependent variations in the results. All bubble images were obtained at a fixed measurement time to avoid temporal fluctuations. The projected bubble-to-water area ratio was calculated from binarized images using consistent threshold values. A^* is defined as the ratio between the area of bubbles generated and the water in the tank. The relationship between the different nozzles and the bubble area ratio A^* is shown in Figure 6. The inlet flow rate Q_w of the water pump is changed by 2 L/min and 3 L/min. The vertical axis in Figure 6 represents the projected bubble-to-water area ratio, which is defined as:

$$A^* = \frac{A_{\text{bubbles}}}{A_{\text{water}}} \tag{4}$$

where $A_{bubbles}$ and A_{water} denote the white (bubbles) and black (water) pixel areas, respectively, in the binarized images. This metric is a two-dimensional projection-based ratio and is therefore presented as a dimensionless value rather than a percentage. All measurements were performed at a fixed time [t = 60 s], and additional tests confirmed that the observed trends are independent of the measurement time.

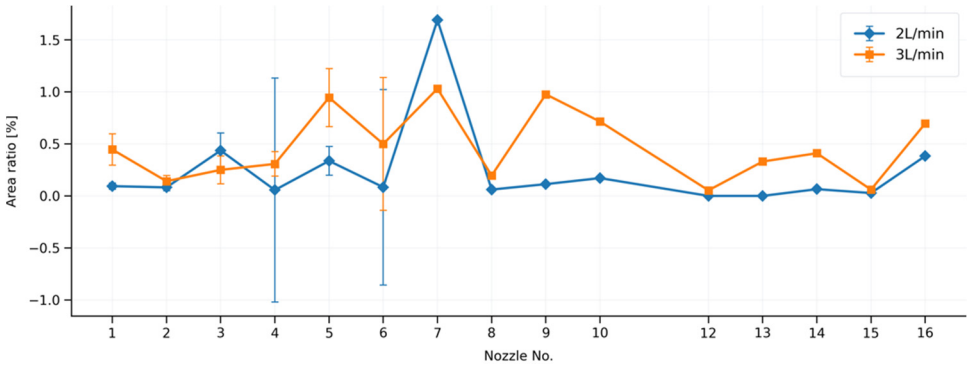

Figure 6. Area ratio (A^*) versus Nozzle No. at two inlet flow rates (2 L/min, 3 L/min). Lines and markers show single-point means. Error bars (where present) denote the standard deviation from a threshold-sensitivity analysis (multiple binarization thresholds near the nominal value) and thus represent methodological uncertainty in image processing rather than experimental variability.

In the figure, at the flow rate of Q_w = 2 L/min, the area ratio A^* is relatively large for Venturi tubes No. 3 and 6. However, at the flow rate of Q_w = 3 L/min, A^* is the largest for Venturi tube No. 6, followed by No. 9 and 5. Also, if we focus on Venturi tube No. 6 in the figure, the area ratio at Q_w = 2 L/min is larger than the one at Q_w = 3 L/min, which differs from the results of the other Venturi tubes. This is due to the larger size of the bubbles generated at a flow rate of Q_w = 2 L/min.

To investigate the minimum size of visual fine bubbles, a microscope is used to photograph the tank filled with fine bubbles, and the minimum diameters of the generated bubbles are calculated by analyzing the sample images. An example of an image taken by the microscope is shown in Figure 7, and the result of the minimum diameters by each nozzle is shown in Figure 8.

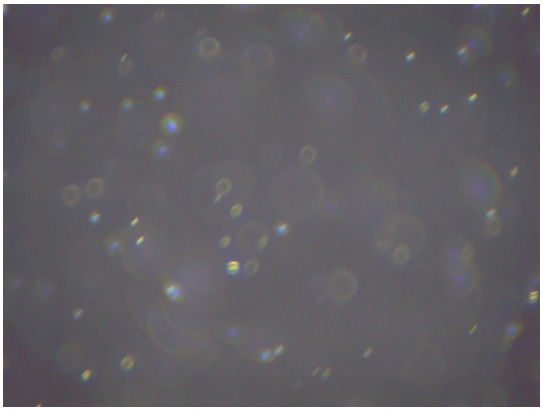

Figure 7. Representative microscopic image of visible fine bubbles in the reservoir. Images were captured with a microscope (model L-KIT652) under consistent optical settings. Scale calibration was performed prior to image processing and subsequent size extraction.

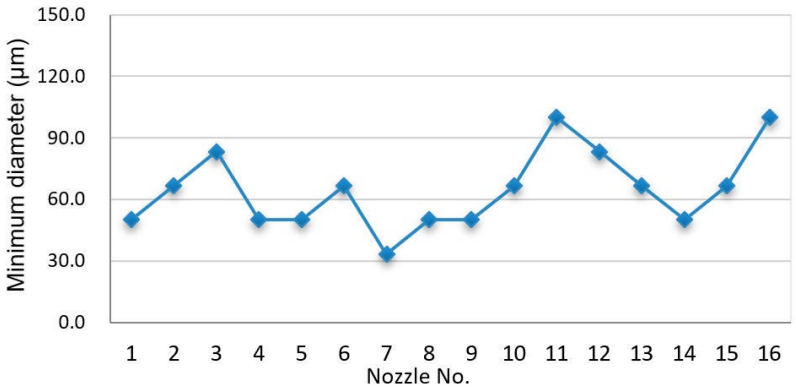

Figure 8. Minimum observed diameter of visible fine bubbles for each nozzle configuration. For each nozzle, multiple microscope images were analyzed, and the smallest reliably resolved bubble diameter was recorded using the same calibration protocol as in Figure 7. The comparison demonstrates geometric effects on the smallest visible bubble size; in particular, the nozzle with a divergent angle of 5° and downstream length of 30 mm (No. 6) yielded the smallest minimum diameter among those tested.

Based on the comparison of the minimum diameters of each nozzle, the minimum diameter of fine bubbles generated by No. 6 is the smallest among them. By simultaneously comparing the volume and particle size of the fine bubbles generated by each nozzle, the No. 6 nozzle achieves the best performance with the largest bubble volume and the smallest particle size. Furthermore, the No. 5 nozzle also shows good performance in terms of volume and bubble size, although it is slightly inferior to No. 6.

3.2. Experiments of Invisible Bubble Measurement

We then focused on the nanobubbles generated by each nozzle. Nanobubble size and concentration were measured using a calibrated Nanosight system following standard NTA procedures. An example of the particle distribution (a) and concentration distribution (b) of nanobubbles generated by the No. 1 nozzle is shown in Figure 9. In the figures, nanobubbles with a size of from 10 to 500 nm are generated with a certain intensity.

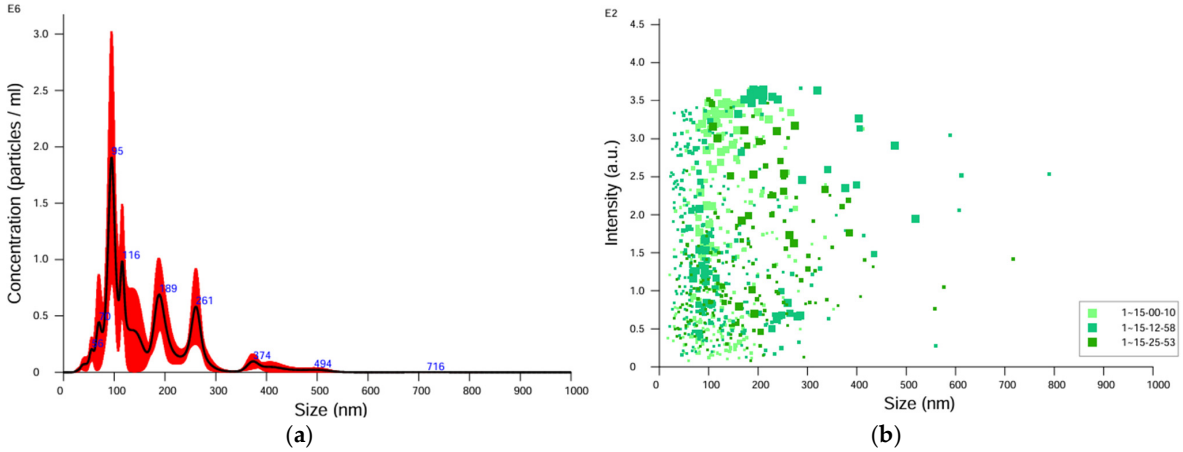

Figure 9. Example nanobubble measurements for Nozzle No. 1 from the nanoparticle tracking analysis (NTA). (**a**) Size–concentration distribution (particles /mL) obtained from FTLA analysis. Thin lines represent three individual measurements, the bold black line shows the mean, and the red shading indicates ±1 standard error (SE) based on the NTA summary statistics. (**b**) Size–intensity distribution (arbitrary units), showing the scattering intensities of individual tracked particles across the same three measurements. Measurement conditions follow the same standard NTA protocol used for Figures 10 and 11.

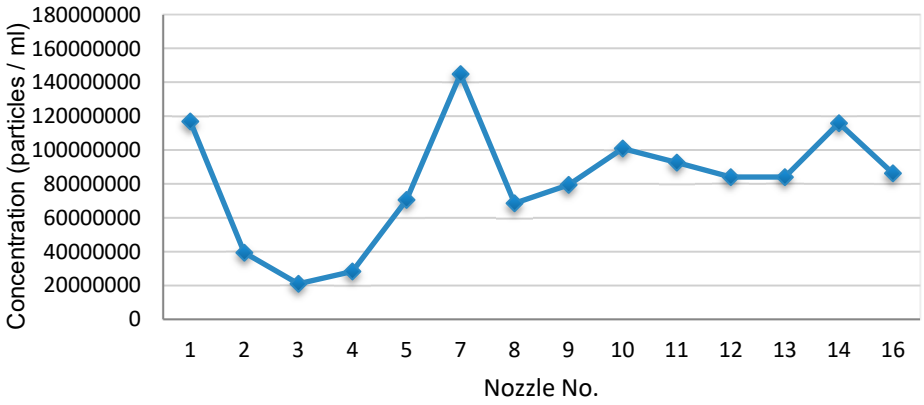

Figure 10. Comparison of nanobubble concentration across nozzle configurations. Samples were collected from the reservoir after steady operation and measured with NTA under identical settings. The figure indicates that Nozzle No. 6 produced the highest nanobubble concentration among all configurations, which is consistent with its high visible-bubble area ratio (Figure 6).

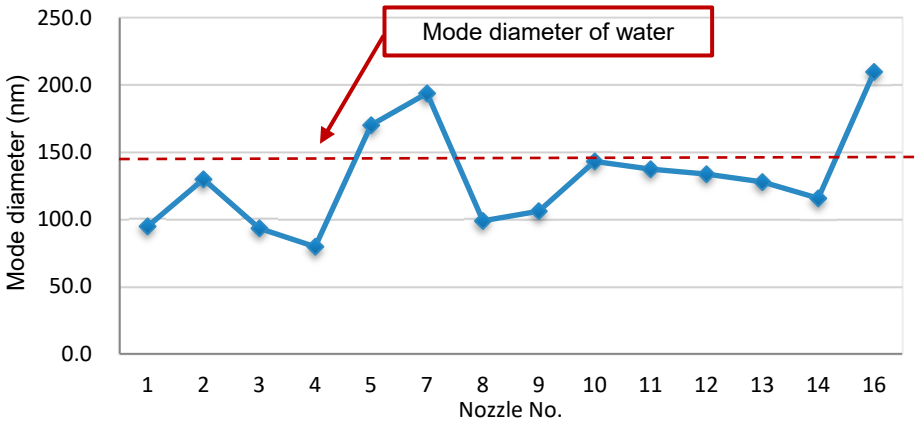

Figure 11. Comparison of nanobubble size distributions (mode diameter) across nozzle configurations. The "mode diameter" is defined as the particle size at which the probability density attains its maximum. For most nozzles (except No. 10), the mode diameter differs significantly from that of tap water, indicating that the measured particles are newly generated nanobubbles rather than pre-existing particulates. Measurements were performed with the same NTA system as in Figures 9 and 10.

The comparison of nanobubble concentrations for each nozzle is shown in Figure 10. From this result, the concentration of nanobubbles generated by the No. 6 nozzle is the highest among all. It also infers that regardless of whether the bubbles are visible, fine, or invisible, the No. 6 nozzle exhibits the highest value compared to the others.

The distribution of particle size of the nanobubbles by each nozzle is shown in Figure 11. The particle size is evaluated by the mode diameter, which is defined as the particle size where the probability density distribution reaches its maximum value. In all of the nozzles except for No. 10, the mode diameters are significantly different from those of tap water. This indicates that the observed bubbles are nanobubbles generated by the nozzles, and not existing bubbles or fine dust in the tap water.

3.3. Experiments on Cleaning Performance

To evaluate the cleaning performance of the fine bubbles, we applied 0.3 g of poster color to the preparation and placed it in the fine bubble water for 1 min at a flow rate of 1 L/min. Then, the weight of the preparation was measured, and the removal rate of the poster color was calculated. In this study, the cleaning performance is defined as the re-

moval efficiency of the colored material deposited on the test plate. The removal efficiency η is calculated as:

$$\eta = \frac{m_{\text{before}} - m_{\text{after}}}{m_{\text{before}}} \quad (5)$$

where m_{before} and m_{after} represent the mass of the plate before and after the cleaning test, respectively. This metric is used in previous experimental studies of bubble-assisted cleaning and represents a widely accepted measure of cleaning performance [15,16].

The images of preparations with poster color before cleaning and after cleaning are shown in Figure 12a,b. The comparison of the removal rates of the fine bubbles from each nozzle and from water is shown in Figure 13.

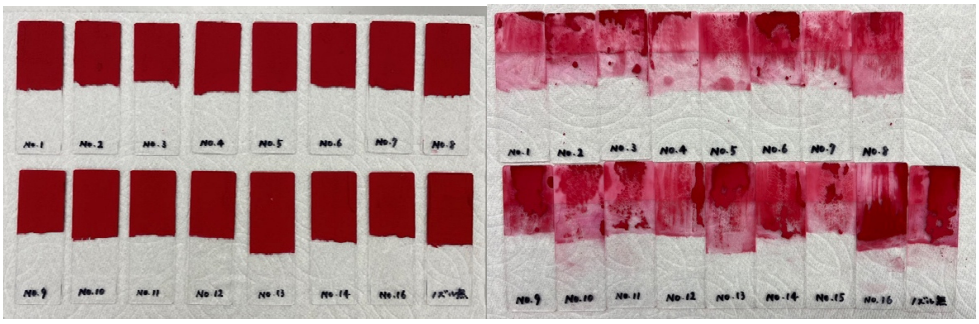

(**a**) (**b**)

Figure 12. Cleaning test specimens before and after exposure to fine bubble water. (**a**) Test plate coated with 0.3 g of poster color prior to immersion; (**b**) the same plate after 1 min of exposure at a flow rate of 1 L /min. The mass difference before and after cleaning is used to compute the removal efficiency (defined in Section 3.3), which serves as the index of cleaning performance used in Figure 13.

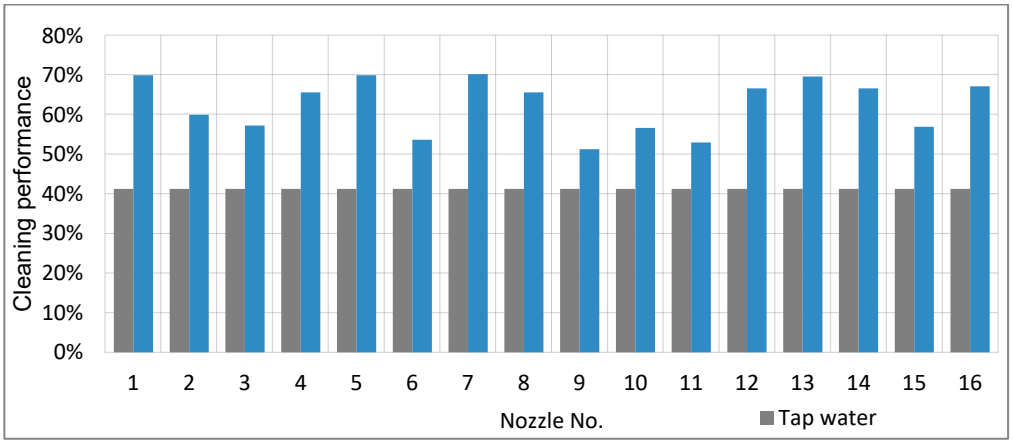

Figure 13. Cleaning performance for fine bubble water versus tap water and across nozzle configurations. Cleaning performance η was calculated from mass measurements of the coated plates (see Figure 12). Blue bars represent fine-bubble water, and gray bars represent tap water. The results show that Nozzle No. 6 achieved the highest removal efficiency (~70.3%), and that fine bubble water nearly doubled the cleaning performance relative to tap water under otherwise identical conditions.

Based on the results, the removal rate of bubbles by the No. 6 nozzle achieves 70.3%, which is the highest among all the nozzles. Additionally, the No. 1, No. 5, and No. 13 nozzles show a relatively high removal rate of 70%. When compared to tap water, the cleaning performance of fine bubble water is nearly twice as high as that of tap water.

We can infer that water with fine bubbles can achieve a remarkable cleaning effect. The cleaning performance depends on the performance of the fine bubbles, including their volume and size, and the geometric parameters have a critical influence on the performance and cleaning

performance of fine bubbles. Among all the Venturi tube nozzles, the No. 5, No. 6, and No. 7 nozzles, with a divergent angle of 5°, exhibit better performance than the others.

Configurations that produce smaller, more numerous bubbles increase the liquid–gas interfacial area and near-wall shear fluctuations in the vicinity of adhered contaminants, which enhances detachment and transport. Consistent with this mechanism, the 5°–30° mm nozzle yields both a high A^* and small bubble sizes (visible and nano-scale), and correspondingly, the highest removal efficiency in our cleaning tests. This link between geometry → bubble population → cleaning performance supports the use of moderate diffuser angles and intermediate lengths in compact oral irrigators.

4. Simulation Results and Analysis

4.1. Void Fraction Distributions

To analyze the flow state inside the Venturi tube for fine bubble generation, we conducted numerical simulations under the same conditions as the experiments. Based on the experimental results, nozzles with a divergent angle of 5°demonstrate better performance compared to others. Therefore, further investigations using simulations were conducted on nozzles No. 4 to No. 7 with a divergent angle of 5°. The simulation results of distributions of void fraction are shown in Figure 14.

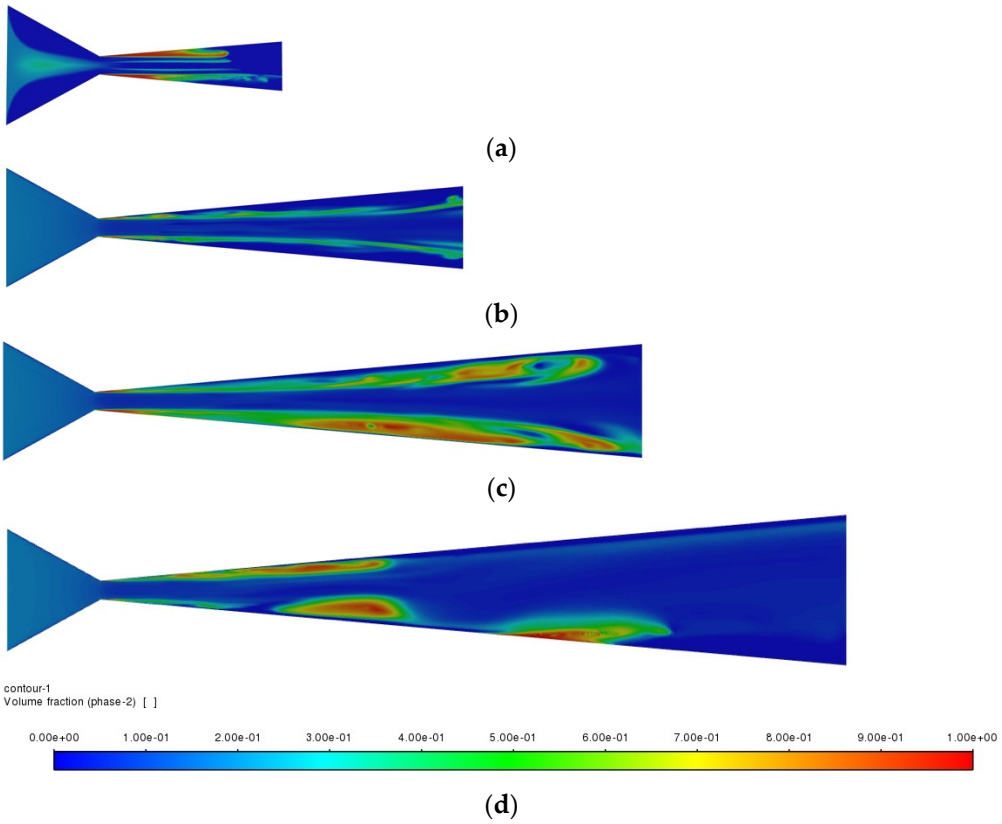

Figure 14. Simulated void fraction distributions for nozzles with a divergent angle of 5°: (**a**) No. 4; (**b**) No. 5; (**c**) No. 6; and (**d**) No. 7. Blue regions indicate continuous liquid (void fraction ≈ 0); darker colors correspond to higher gas volume fraction. Bubbles separate at the throat and accumulate downstream near the wall, with the spatial extent and intensity depending on the downstream length. Among these cases, Nozzle No. 6 shows the broadest region of elevated void fraction, consistent with the experimental trends in Figure 6.

The areas filled with blue represent water with a void fraction of 0, while the darker-colored areas represent air with a void fraction ranging from 0 to 1. It can be observed that when the gas–liquid two-phase flow passes through the throat part, many bubbles

separate from the water and accumulate near the wall in the downstream section of the throat. Then, the bubbles are broken up into numerous tiny fragments due to strong deformation of phase boundaries under various kinds of force, including pressure gradient force, drag force, buoyancy, lift, and virtual mass force [10]. Among all the Venturi tube nozzles, No. 6 produces the largest volume of bubbles, which is consistent with the experimental results. Furthermore, the locations where bubbles accumulate vary with changes in the length of the downstream section. In Nozzle No. 4, a large number of bubbles are generated immediately after the throat, near the downstream wall of the throat. While in No. 6, the bubbles are distributed throughout the downstream part of the throat.

4.2. Turbulence Energy Distributions

The turbulence energy distributions that promote the breakup of bubbles at different nozzles are illustrated in Figure 15. The turbulence energy increases as the color changes from blue to red. In Figure 15, we can see that when the divergent angle is the same, the distribution of turbulence energy is similar, and the position of the strongest turbulence energy is almost identical. Compared to the void fraction distribution, when a large number of bubbles gather in the strong turbulent area, bubble breakup becomes intense, and a lot of tiny bubbles are generated. However, in Nozzle No. 4, the bubble gathering location is different from the area with the strongest turbulence energy. Therefore, the breakup of bubbles is not as intense, and the volume of fine bubbles is small. On the other hand, in Nozzle No. 6, a lot of bubbles are generated in the downstream section, and the bubble gathering location aligns with the area of strongest turbulence energy. As a result, a large number of small fine bubbles are generated. The geometric parameters determine both the bubble generation location and the distribution of turbulence energy, indicating that there are optimized geometric parameters for Venturi tubes in fine bubble generation.

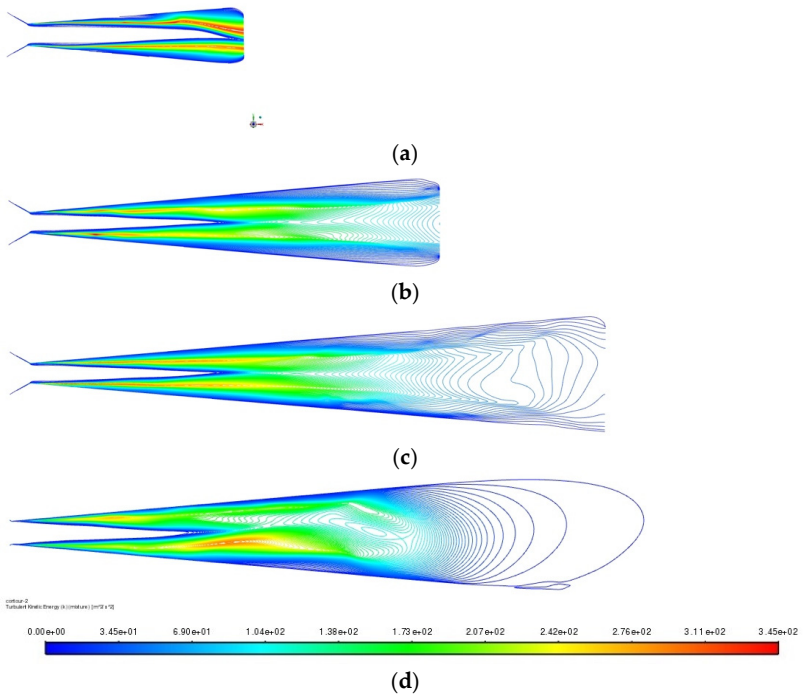

Figure 15. Simulated turbulence energy distributions for the same four nozzles: (**a**) No. 4; (**b**) No. 5; (**c**) No. 6; and (**d**) No. 7. Color progression from blue to red denotes increasing turbulence kinetic energy. For identical divergent angles, the location of peak turbulence is similar across cases; performance differences arise from how bubble-rich regions (Figure 14) align with high-energy zones. Nozzle No. 6 exhibits strong overlap between bubble clusters and high turbulence, promoting intensified breakup and smaller bubble sizes.

An example of the wall pressure distribution in Nozzle No. 5 is shown in Figure 16. The theoretical value is calculated by the following Equation (6) of Bernoulli's principle [11]. In this figure, there is a pressure loss in the outlet between the theoretical value and the simulation value, which is considered the energy for bubble breakup. The pressure loss is also affected by the geometric parameters of Venturi tubes.

$$\frac{p_i}{\rho g} + \frac{{v_i}^2}{2g} + z_i = \frac{p}{\rho g} + \frac{v^2}{2g} + z \quad (6)$$

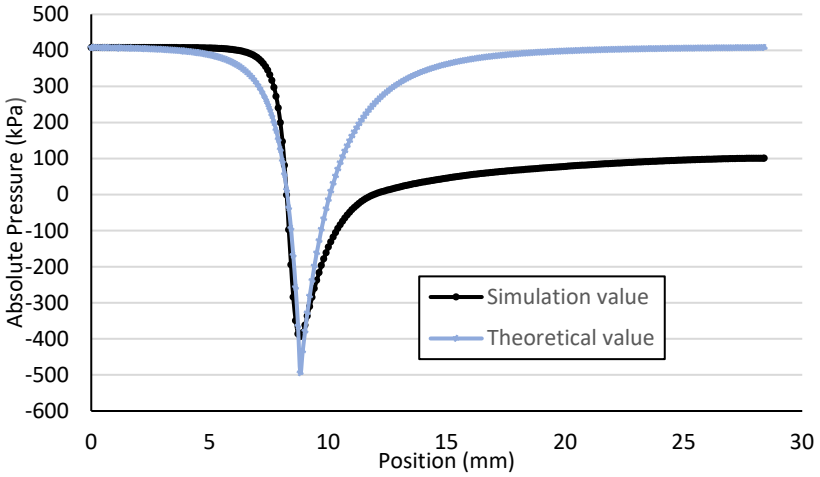

Figure 16. Wall pressure distribution along Nozzle No. 5 and comparison with the theoretical profile from Bernoulli's principle. The simulation indicates a pressure shortfall at the outlet relative to the inviscid theoretical curve, representing energy dissipated by turbulence and bubble breakup. This loss and its dependence on geometry help explain variations in bubble generation efficiency observed experimentally.

4.3. Bubble Diameter Distributions

The distributions of bubble diameters in the central cross-section of each nozzle are shown in Figure 17. The color change from blue to red corresponds to the variation in diameters from the minimum to the maximum. The results show that the coalescence and breakup of bubbles occur in the divergent section of each nozzle. In addition, the locations of coalescence and breakup are different when the length of the divergent part changes, even though the divergent angle remains the same.

4.4. General Effects of Micro-Nozzle Geometry

When comparing nozzles at a fixed downstream length, increasing the divergent angle from ~2.5° to ~5° increased the projected bubble-to-water area ratio (A^*) and decreased both the minimum visible diameter and the nanobubble mode diameter. Further increasing the angle to ⌾7.5–12.5°reduced A^* and enlarged the characteristic bubble sizes, indicating performance degradation at higher angles.

At a fixed angle, extending the downstream length from 10 mm to 30 mm improved A^* and reduced bubble sizes; extending further to 40 mm did not yield additional gains and in some cases slightly worsened the metrics. The 5°–30° mm configuration reproducibly delivered a high A^* together with small visible and nano-scale bubbles, suggesting that moderate diffusion (angle) over an intermediate residence length enhances breakup while avoiding premature coalescence.

The void fraction and turbulence energy fields show that, for 5°–30° mm, bubble clusters form and persist within a high-turbulence corridor downstream of the throat, promoting repeated breakup. In contrast, shorter lengths shift clusters upstream where the energy peak is misaligned, while larger angles promote rapid expansion and weakened shear, both of which

limit sustained breakup and favor coalescence. This alignment between bubble cluster location and turbulence peak explains the observed geometry–performance trends.

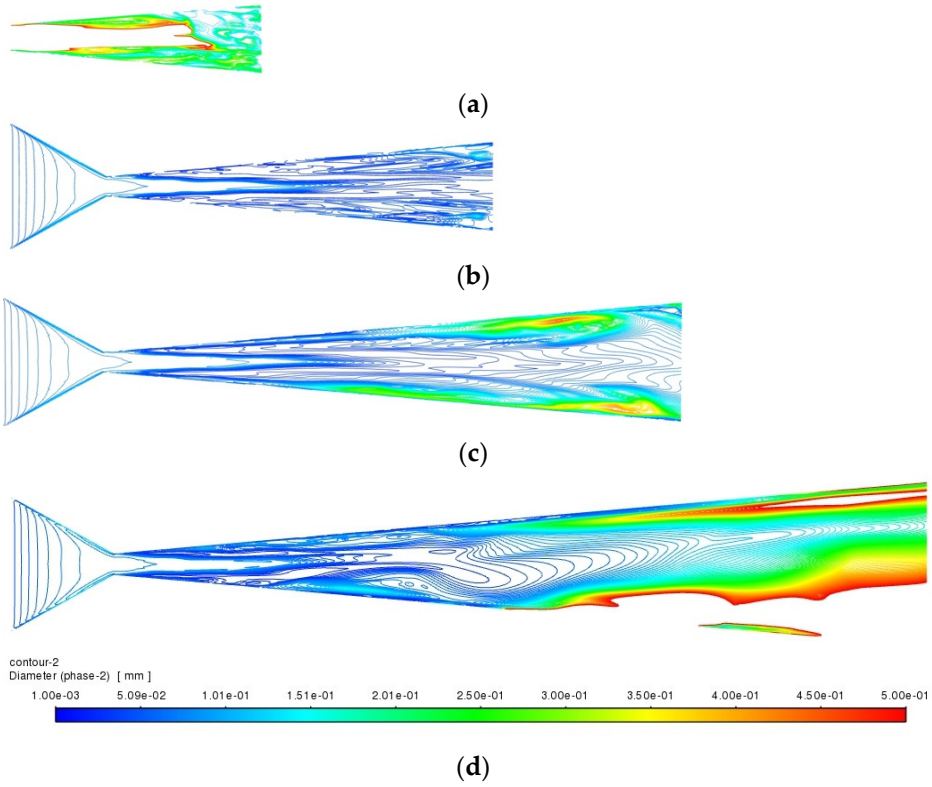

Figure 17. Simulated bubble diameter distributions on the central cross-section for: (**a**) No. 4; (**b**) No. 5; (**c**) No. 6; and (**d**) No. 7. Color maps encode the local characteristic bubble diameter from the population balance model; blue denotes smaller and red larger sizes. Breakup and coalescence primarily occur in the divergent section. Changing the downstream length shifts the regions of coalescence/breakup even at the same angle, with Nozzle No. 6 showing the most extensive small-diameter zone, aligning with the experimental performance in Figures 6, 8, 10 and 11.

Taken together, the general effect of micro-nozzle geometry can be summarized as follows:

(i) Too small a divergent angle or too short a downstream length under-utilizes turbulent breakup.
(ii) Too large an angle or too long a length weakens shear and/or increases coalescence probability.
(iii) A moderate angle (~5°) and an intermediate length (~30 mm) balance shear-induced breakup and residence time, yielding higher bubble production (A^*) and smaller sizes across both visible and nano-scales in our operating range.

5. Conclusions

In this work, Venturi tube fine bubble generators were designed to be embedded in an oral irrigator utilizing fine bubble technology for oral purification. Venturi tubes with different geometric combinations were developed to improve the performance of fine bubble generation, including bubble size and volume, through experiment and numerical simulation. Both the experimental and simulation results show that the generation performance and cleaning performance depend on the geometrical parameters of the Venturi tube, and the Venturi tube with a divergent angle of 5° and a divergent length of 30 mm demonstrates the best performance compared to others. The simulation results show that bubble

breakup occurs in the downstream section of the Venturi tube. When the bubbles concentrate in areas with intense turbulence energy, a large number of small fine bubbles are generated. The geometric parameters determine both the bubble generation location and the distribution of turbulence energy.

Supplementary Materials: The following supporting information can be downloaded at: https://www.mdpi.com/article/10.3390/fluids11030063/s1, Video S1: High-speed video visualization inside the nozzle under a flow rate of 2 L/min. Video S2: High-speed video visualization inside the nozzle under a flow rate of 1.5 L/min

Author Contributions: Conceptualization, X.J. and S.O.; methodology, X.J.; experiment, X.J., R.M., Y.O. and M.S.; validation, X.J., R.M., M.S. and S.O.; resources, S.O.; data curation, X.J.; simulation, X.J.; writing—original draft preparation, X.J.; writing—review and editing, Y.O. All authors have read and agreed to the published version of the manuscript.

Funding: This research was funded by Takahashi Industrial and Economic Research Foundation (公益財団法人 高橋産業経済研究財団).

Institutional Review Board Statement: Not applicable

Informed Consent Statement: Not applicable

Data Availability Statement: The original contributions presented in this study are included in the article/Supplementary Materials. Further inquiries can be directed to the corresponding author.

Acknowledgments: We gratefully acknowledge the support of Prof. Katsuro Tachibana of Fukuoka University for conducting the particle size analysis experiments.

Conflicts of Interest: Author Satoru Ogahara was employed by the company Hoyo Seisakusho Co., Ltd. The remaining authors declare that the research was conducted in the absence of any commercial or financial relationships that could be construed as a potential conflict of interest.

Abbreviations

The following abbreviations are used in this manuscript:

CFD	Computational Fluid Dynamics
NTA	Nanoparticle Tracking Analysis
PBM	Population Balance Model
VOF	Volume of Fluid

References

1. Ministry of Economy, Trade and Industry, Kyushu Bureau of Economy, Department of Natural Resources, Energy and Environment. *Fine Bubble Utilization Case Study Collection*; Organization of METI-KYUSHU: Fukuoka City, Japan, 2018.
2. Huang, J.; Sun, L.; Du, M.; Mo, Z.; Zhao, L. A visualized study of interfacial behavior of air–water two-phase flow in a rectangular Venturi channel. *Theor. Appl. Mech. Lett.* **2018**, *8*, 334–344. [CrossRef]
3. Wilson, D.A.; Pun, K.; Ganesan, P.B.; Hamad, F. Geometrical Optimization of a Venturi-Type Microbubble Generator Using CFD Simulation and Experimental Measurements. *Designs* **2021**, *5*, 4. [CrossRef]
4. Huang, J.; Sun, L.; Liu, H.; Mo, Z.; Tang, J.; Xie, G.; Du, M. A review on bubble generation and transportation in venturi-type bubble generators. *Exp. Comput. Multiph. Flow* **2020**, *2*, 123–134. [CrossRef]
5. Zhao, L.; Sun, L.; Mo, Z.; Du, M.; Xie, G.; Tang, J. An investigation on the effect of divergent angle on performance of Venturi-type bubble generators. In *Deep Rock Mechanics*; CRC Press: Boca Raton, FL, USA, 2018.
6. Nadumaran, N.; Alias, E.A. Effect of divergent angle and water flowrate on mean bubble size in venturi-type generator: An experimental and computational approach. *J. Mech. Eng. Sci.* **2025**, *19*, 10667–10675. [CrossRef]
7. Zhao, L.; Sun, L.; Mo, Z.; Du, M.; Huang, J.; Bao, J.; Tang, G.; Xie, G. Effects of the divergent angle on bubble transportation in a rectangular Venturi channel and its performance in producing fine bubbles. *Int. J. Multiph. Flow* **2019**, *114*, 192–206. [CrossRef]
8. Feng, Y.; Mu, H.; Liu, X.; Huang, Z.; Zhang, H.; Wang, J.; Yang, Y. Leveraging 3D Printing for the Design of High-Performance Venturi Microbubble Generators. *Ind. Eng. Chem. Res.* **2020**, *59*, 8447−8455. [CrossRef]

9. Li, J.; Song, Y.; Yin, J.; Wang, D. Investigation on the effect of geometrical parameters on the performance of a venturi type bubble generator. *Nucl. Eng. Des.* **2017**, *325*, 90–96. [CrossRef]
10. Jiang, X.; Yasunobu, T.; Nakamura, A.; Shimazu, M. Miniaturization of Bubbles by Shock Waves in Gas-Liquid Two-phase Flow in the Venturi Tube. *J. Therm. Sci.* **2021**, *30*, 1068–1076. [CrossRef]
11. Nadumaran, N.; Alias, E. AImpact of Throat Diameter, Length, and Divergent Angle on Bubble Formation and Flow Characteristics in Venturi Microbubble Generators. *Int. J. Automot. Mech. Eng.* **2025**, *22*, 12933–12942. [CrossRef]
12. Gänzer, H.; Kasslatter, M.; Wiesmüller, V.; Denk, L.; Sigwart, A.-M.; Crismani, A. Cleansing efficacy of an oral irrigator with microburst technology in adolescent orthodontic patients: A randomized-controlled crossover study. *Clin. Oral Investig.* **2024**, *28*, 524. [CrossRef] [PubMed]
13. Lin, P.-J.; Chuang, M.-C.; Chang, S.-C. Research on the cleaning efficacy of micro-bubbles on dental plaque. *Procedia Manuf.* **2015**, *3*, 13–20. [CrossRef]
14. Available online: https://www.qd-japan.com/products/nanosight/ (accessed on 22 September 2022).
15. Ma, X.-T.; Li, M.-B.; Sun, C. Measurement and characterization of bulk nanobubbles by nanoparticle tracking analysis. *J. Hydrodyn.* **2022**, *34*, 1121–1133. [CrossRef]
16. Moleaer. How to Measure, View and Study Nano-Sized Bubbles (Tech Blog, 2023). Available online: https://www.moleaer.com/blog/nanobubbles/measure-view-study-nanobubbles (accessed on 20 December 2024).
17. Ansys Fluent User's Guide, *Population Balance Model (PBM)—Setup & Theory*; Ansys: Canonsburg, PA, USA, 2011.
18. Ansys CFX Theory Guide, *Luo and Svendsen Breakup Model (MUSIG)*; Ansys: Canonsburg, PA, USA, 2011.
19. Available online: https://www.afs.enea.it/project/neptunius/docs/fluent/html/popbal/main_pre.htm (accessed on 20 December 2024).
20. Reichmann, F.; Tollkötter, A.; Körner, S.; Kockmann, N. Gas-liquid dispersion in micronozzles and microreactor design for high interfacial area. *Chem. Eng. Sci.* **2017**, *169*, 151–163. [CrossRef]
21. Batchelor, G.K. *An Introduction to Fluid Dynamics*; Cambridge University Press: Cambridge, UK, 2000; ISBN 978-0-521-66396-0.

Disclaimer/Publisher's Note: The statements, opinions and data contained in all publications are solely those of the individual author(s) and contributor(s) and not of MDPI and/or the editor(s). MDPI and/or the editor(s) disclaim responsibility for any injury to people or property resulting from any ideas, methods, instructions or products referred to in the content.